PROGRESS IN PHOTOVOLTAICS: RESEARCH AND APPLICATIONS
Prog. Photovolt: Res. Appl. 2015; **23:**403–416
Published online 17 December 2013 in Wiley Online Library (wileyonlinelibrary.com). DOI: 10.1002/pip.2435

RESEARCH ARTICLE

Design of a polymer optical fiber luminescent solar concentrator

Esmaeil-Hooman Banaei[1,2] and Ayman F. Abouraddy[1] *

[1] Center for Research and Education in Optics and Lasers (CREOL), The College of Optics & Photonics, University of Central Florida, Orlando, FL 32816, USA
[2] Department of Electrical Engineering and Computer Science, University of Central Florida, Orlando, FL 32816, USA

ABSTRACT

We present the design and optimization of a polymeric optical fiber luminescent solar concentrator (FLSC) and systematically investigate the impact of the geometrical and physical parameters of the fiber and active luminescent dopants on the FLSC performance. A multiplicity of individual FLSCs may be arranged on a surface to form a low-weight and mechanically flexible solar concentrating fabric. In addition to these unique structural properties, we find that the overall optical-to-electrical conversion efficiency of the FLSC rivals that of reported flat slab LSCs while increasing the geometric gain, thereby potentially reducing the cost. Copyright © 2013 John Wiley & Sons, Ltd.

KEYWORDS
luminescent solar concentrators; polymer fibers

***Correspondence**
Ayman F. Abouraddy, Center for Research and Education in Optics and Lasers (CREOL), The College of Optics & Photonics, University of Central Florida, Orlando, FL 32816, USA.
E-mail: raddy@creol.ucf.edu
†Now at Flex Optronix Technologies, LLC.

Received 19 December 2012; Revised 26 May 2013; Accepted 15 September 2013

1. INTRODUCTION

Luminescent solar concentrators (LSCs) are a promising alternative for reducing the cost of solar energy [1]. LSCs are optical waveguide structures doped with luminescent materials such as organic dyes [2], quantum dots [3,4], or inorganic rare-earth ions [5], which are either embedded in the structure [6,7] or coated on top of it [2] to absorb incident sunlight. Luminescence emitted into the waveguide modes reaches photovoltaic (PV) cells placed at the structure edges. LSCs thereby reduce the area of the PV cells used and may become economically viable when the cost-efficiency of LSC manufacturing improves upon that of PV cells.

The LSC concept may be traced back to an unpublished proposal (see Ref. [6]) but became known through the work of Weber and Lambe [8]. The recent surge of interest in solar energy driven by geopolitical factors, environmental fears, and the prospect of a dwindling fossil-fuel supply has rekindled interest in LSCs. It has become useful to distinguish a first generation (Gen1) of LSCs developed in the 1970s and 1980s from a recent second generation (Gen2) that benefits from advances in luminescent materials, optical polymers, and the fabrication of optical waveguide structures [1,9]. For example, luminescent materials with wide absorption bands and low self-absorption rates, such as quantum dots, have improved LSC efficiencies [3,10,11]; alignment of luminescent molecules has increased the directional coupling of their radiation into guided modes [12–14]; and inter-molecular energy transfer schemes have reduced self-absorption [2]. As a result, the conversion efficiency of LSCs has topped 7.1% for small-area, but relatively thick, samples ($5 \times 5 \times 0.5$ cm^3) [15]. Other improvements include exploring different waveguide geometries [16], patterning the luminescent material doping [17], improving the LSC-to-PV coupling using plasmonic particle resonances [18], fluorescence resonant shifting [19], and embedding silicon micro-PV cells in the LSC to reduce self-absorption [20].

Another emerging class of Gen2 LSCs exploits non-traditional waveguide *form-factors* such as cylindrical light pipes, which may have higher concentration efficiencies compared with slab waveguides [9,21], and may thus enable solar energy harvesting in new contexts. Along this

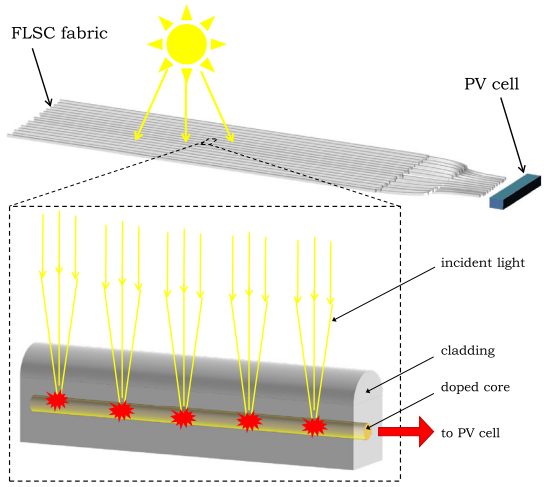

Figure 1. Overall design of a fiber luminescent solar concentrator (FLSC) system with individual fibers assembled in a fabric. The fiber ends are bundled and connected to a small-area photovoltaic (PV) cell. The inset highlights a single FLSC having the cross section shown in Figure 2(c). Incident sunlight is focused into luminescent dopants, and a percentage of the emitted light is trapped in the fiber and propagates to the fiber end.

vein, solar concentration via laser-dye-doped optical fibers was recently suggested but without reporting efficiency measurements [22]. The use of polymer optical fibers to realize flexible and low-weight LSCs may enable solar energy harvesting in mobile applications.

In this paper, we describe the design, detailed numerical simulation, and optimization of a fiber LSC (FLSC) in which a *polymer* optical fiber judiciously impregnated with luminescent dopants absorbs sunlight incident externally on its outer surface. The fiber then plays the role of a waveguide for transmission of this luminescence to the fiber end where PV cells are placed. Figure 1 depicts schematically the overall FLSC system configuration. A multiplicity of individual parallel FLSCs is assembled on a surface, and their ends are bundled and connected to a small-area PV cell. Each fiber is an independent LSC, and their juxtaposition enables covering a large surface area. The geometric gain [2], defined as the ratio of the area covered by the LSC to the area of the PV cells required, is approximately the ratio of the fiber length to its diameter, which can be considerably high. Such structures may potentially lead to wearable solar-harvesting fabrics for mobile energy.

The specific class of fibers we investigate here has a non-traditional structure: its cross section comprises a rectangle with an axially symmetric cylindrical cap on the top surface designed to focus externally incident light into the fiber (Figure 2(c)). Luminescent dopants, located at the focal spot (extending axially along the fiber), absorb incident sunlight and re-emit light into the fiber, which is then guided to the fiber end. Fiber-based LSCs with uniform luminescent doping results in high self-absorption, while coating the dopants on the fiber surface, as is usually performed in flat LSCs, eliminates the benefits accrued by the curved fiber surface. The FLSC design we investigate here harnesses the focusing capabilities of the curved fiber surface to minimize the amount of dopants needed, thereby reducing self-absorption. To the best of our knowledge, this is the first time that an FLSC design has been systematically investigated and optimized for efficient LSC. Furthermore, we demonstrate experimentally the feasibility of producing such non-traditional fiber structures using the traditional process of thermal fiber drawing from a scaled-up model called a "preform" (Figure 2) [23].

Previous theoretical studies have examined LSC performance from various viewpoints, such as microscopic-level models based on molecular light-matter interactions [24], thermodynamic approaches based on radiative transfer theory from a macroscopic perspective [25], and system-level design and optimization using Monte Carlo ray tracing. Here, we primarily employ the ray-tracing method for optical system design, analysis, and optimization (see the Appendix for details).

The paper is organized as follows. After providing an overview of the general strategy in Section 2, we elucidate the rationale for choosing the rectangular fiber with an integrated cylindrical lens cap in Section 3 by comparing it with two simpler structures, rectangular and cylindrical waveguides, along with our experimental progress on controllably fabricating "cold" polymer fibers (i.e., undoped) with cross-sectional structures similar to those studied theoretically here. Section 4 examines the first stage of the concentration process, absorption of incident sunlight, and evaluates the dependence of absorption efficiency on the fiber geometrical and physical degrees of freedom. In Section 5, we investigate the capture of the luminescence in the fiber via total internal reflection (TIR), while Section 6 focuses on the important issue of self-absorption as a limiting factor for increasing the length of FLSCs (and hence setting a limit on the geometrical gain). We conclude Section 6 with a simple empirical model of the dependence of self-absorption on the fiber degrees of freedom, allowing for rapid evaluation of multiple designs. Section 7 presents results on optimizing the performance of the proposed FLSC over the full parameter space of the FLSC structural and physical degrees of freedom. Up to this point, the analysis is carried out using a fixed pair of absorption and emission wavelengths. We lift this restriction in Section 8, where we present an analysis that takes into consideration the solar spectrum and the wavelength dependence of absorption and luminescence by a dopant. We conclude the paper by summarizing the potential advantages of FLSCs with respect to traditional LSC designs.

2. OVERALL STRATEGY

Although optical glasses may attain superior optical properties with respect to polymers, thereby making them useful in the construction of LSCs, polymers have the pos-

DOI: 10.1002/pip

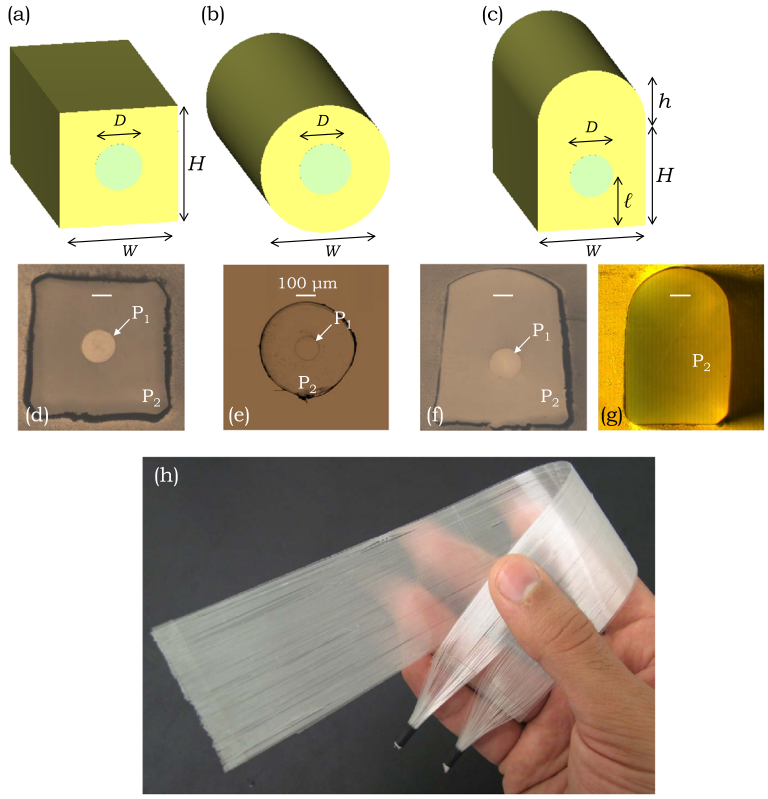

Figure 2. Schematic cross sections of three fiber luminescent solar concentrator (FLSC) structures: (a) a square fiber, (b) a traditional cylindrical fiber, and (c) a rectangular fiber with a cylindrical cap on the top surface. In all three cases, a cylindrical core region is doped with luminescent materials. (d)–(g) Transmission optical micrographs of physical examples of drawn "cold" polymer fibers (i.e., undoped) corresponding to (a)–(c). (f) and (g) are hybrid fiber structures with different cylindrical cap height; there is no core in (g). The fibers are made of cyclic olefin polymer (P_2), and the undoped core region is polycarbonate (P_1). Scale bars are all 100 μm. (h) is a prototype FLSC fabric assembled from multiple "cold" fibers on a thin polymer film.

itive attributes of easier processing and machining, lower price, higher mechanical flexibility and robustness, and lower weight. Optical polymers thus offer a compromise between these useful attributes and optical performance. Polymers, such as cyclic olefin polymer (COP), are highly transparent in the visible and can demonstrate high photostability with low absorption in the ultraviolet [26]. A subset of optical polymers, typically *thermoplastic* polymers such as COP, may be thermally drawn into fibers, and they are natural candidates for fabricating FLSCs.

From the schematic depiction in Figure 1, we may divide the operation of an FLSC into three distinct steps:

(1) *Absorption of sunlight in the fiber*. Sunlight incident on the external surface of the FLSC is focused by its curved outer surface into a preselected spot inside the fiber where luminescent dopants are placed. The fraction of incident sunlight absorbed in the fiber may be maximized through optimizing the fiber surface geometry, transverse structure, and concentration and spatial distribution of the luminescent dopants (Sections 3 and 4).

(2) *Luminescence capture by the fiber*. A fraction of the emitted luminescence is captured by TIR, depending on the refractive index and structure of the FLSC (Section 5). This captured fraction further depends on the orientation distribution of the radiating dipoles, which may indeed be enhanced if the dopants are engineered in such a way that preferential radiation along the waveguide is achieved. This would result in excluding more luminescence from the escape cone and hence a higher capture efficiency [12,27,28]. In this study, nevertheless, we have restricted our simulations to the generic case of isotropic radiation to provide conservative efficiency bounds.

(3) *Optical emission delivery*. The captured luminescence undergoes absorption as it propagates along the fiber, mainly due to self-absorption. This issue is investigated in Section 6 where we examine the effects of the FLSC degrees of freedom on light transport efficiency.

The distribution and concentration of the luminescent dopants must be chosen to strike a compromise between

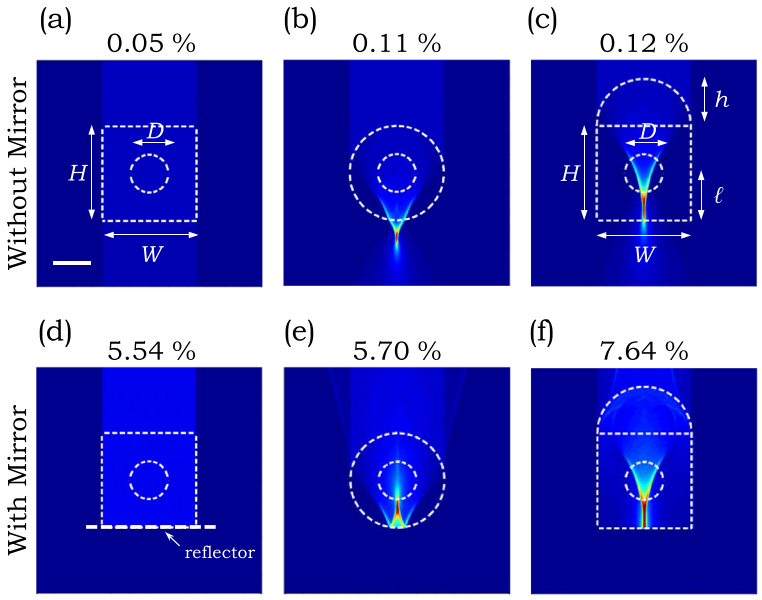

Figure 3. Ray-tracing simulations of normally incident light in the three "cold" (undoped) structures shown in Figure 2. In (a)–(c) there is no back-reflector below the fiber structures. In the second row (d)–(f), a flat reflective surface is placed under the fiber (thick dashed horizontal line). Panels (a) and (d) correspond to a rectangular fiber, panels (b) and (e) to a cylindrical fiber, and panels (c) and (f) to the hybrid fiber structure we consider in this paper. The thin dashed white lines highlight the structure, and the dashed circle in the middle of each structure corresponds to where the doped core ($D = 200$ μm) will be placed and is here only a guide to the eye. Scale bar is 200 μm. The number in each panel is the percentage of light absorbed due to polymer loss and finite reflectivity of the back mirror (see text for details).

increasing optical absorption and decreasing the self-absorption, which sets the limit on luminescence propagation along the fiber to the PV cell. We carry out this optimization in Section 7. Finally, optical-to-electric energy conversion occurs at the fiber tips that are coupled to a PV cell optimized with respect to the luminescence spectrum and not the full solar spectrum. The mechanical flexibility and robustness of polymer fibers allows bundling them together at their ends, which facilitates interfacing them to PV cells (Figure 2(h)).

3. GENERAL FIBER DESIGNS

We start by comparing three broad classes of polymer fiber structures: (i) rectangular fibers (dimensions $W \times H$) that resemble traditional flat LSCs (Figure 2(a)); (ii) cylindrical fibers with outer diameter W (Figure 2(b)); and (iii) hybrid fibers consisting of a rectangular cross section ($W \times H$) with an axially extending cylindrical cap of height h and radius of curvature $r = (h/2) + (W^2/8h)$ on top (Figure 2(c)). In all three fibers, the luminescent dopants are located in a "core" of diameter D, whose center is at a height ℓ in the hybrid structure and is located at the geometric center in the rectangular and cylindrical structures. The refractive index is uniform over the cross section, and the doped core differs only in that it has an optical density of α_d (in absorbance units per centimeter). The optical density is a measure of absorbance of light transmitted through an absorbing material that varies with material thickness and concentration of the dopants. Here, we characterize optical density with absorbance per unit thickness of the dopants absorbing material (abs. units/cm thereon). Light propagating through a material of thickness ℓ (in centimeter) and having optical density α_d (abs. units/cm) undergoes attenuation by a factor $e^{-\alpha_d \ell}$.

We consider a generic polymer with refractive index $n = 1.53$ and optical absorption losses 1 dB/m [29]. Such parameters are comparable with those of typical optical polymers such as COP [26] or polycarbonate (PC) [30]. We compare the focusing capabilities of the fiber external surfaces by examining the "cold" fiber structures, that is, in the absence of luminescent dopants. In Figure 3, we plot the results of the ray-tracing simulations of light incident vertically with respect to the horizontal axis of cold fibers suspended in air (see the Appendix for details).

The rectangular fiber (Figure 3(a); 500×500 μm^2) does not focus incident light, and the fraction of sunlight intercepted by the core is at best D/W. In the cylindrical fiber (Figure 3(b); $W = 500$ μm), the external curved surface focuses incident rays to the opposing side of the fiber, and the percentage of rays intercepted by the core is now larger than D/W. This outcome is *independent* of the fiber diameter: The focal point is *always* at the opposite side of the fiber (for typical values of n). In the hybrid fiber structure (Figure 3(c)), a cylindrical cap is provided on the top that focuses incident light to a point inside the fiber determined by its curvature. For example, if the cap is a half cylinder of diameter W, $h = W/2$, then incident light is focused into the

DOI: 10.1002/pip

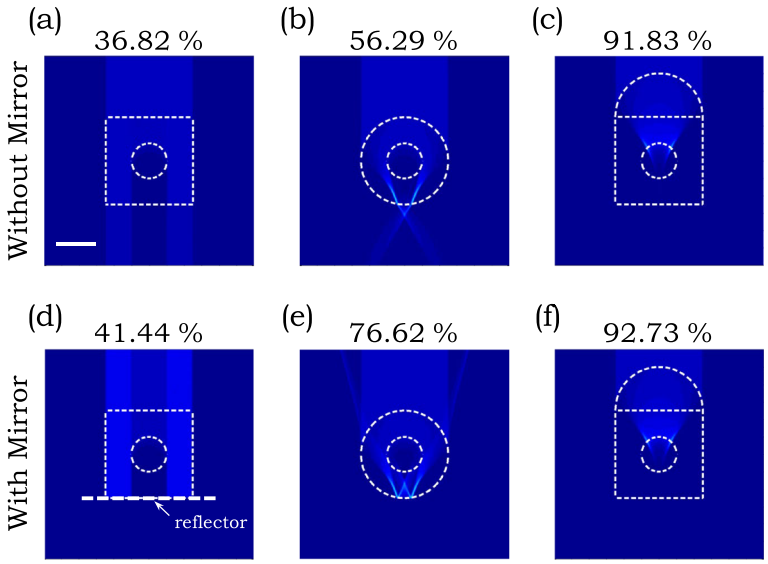

Figure 4. Ray-tracing simulations of normally incident light in the three "hot" structures shown in Figure 2 (cores are doped, in contrast to the "cold" structures in Figure 3); $\alpha_d = 100$ cm^{-1} in the core, and core diameters are all $D = 200$ μm. The panels (a) through (f) correspond to those in Figure 3, except that a doped core is added. The number in each panel is the *total* percentage of light absorbed in the fiber. In the second row, a reflective surface is placed below the fiber. Dashed white lines provide an outline for the structure and the doped core. Scale bar is 200 μm.

core (Figure 3(c); $W = H = 500$ μm). This structure therefore allows one to choose the location of the spot at which externally incident light is focused by judiciously choosing W, H, and h, in contradistinction to the cylindrical fiber where the location of the focal spot is predetermined (see Ref. [31] for a similar concept implemented in a planar device). In addition, using such a structure facilitates assembling the fibers on a surface while maintaining correct orientation, enables a large fill-factor, and potentially allows placing a back reflector beneath the FLSC assembly.

It is useful to consider the effect of adding a reflector under the three fiber structures (Figure 3(d)–(f)). We model the reflector as an aluminum coating with complex refractive index $n = 0.7 - 7.0i$ giving a 94.6% reflectivity for normal incidence. The mirror is separated from the fiber by a thin air gap (1 μm thick; results are not sensitive to the gap thickness). In this way, by varying the cap height h, it may be arranged for incident light to pass through the core twice. (See the Appendix for a further discussion of the impact of such a back reflector on the proposed structures.)

With our understanding of the trajectories of the light rays in the "cold" structures, we proceed to determine the fraction of incident light absorbed by luminescent materials in doped cores ($\alpha_d = 100$ cm^{-1}). Figure 4 shows that the fraction of incident light absorbed is strongly dependent on the surface geometry. In the square fiber (Figure 4(a)), the amount of captured light is approximately $D/W = 0.4$, as expected. The absorption is highest in the capped fiber (Figure 4(c)). Although it is conceivable that more complex surface structures may outperform this one, we limit ourselves here to fibers having axial symmetry, because they can be drawn from a macroscopic preform by traditional thermal drawing [23] and do not require post-processing.

Note that the geometric gain G in a traditional flat LSC of dimensions $L \times L$ and thickness H is defined as the ratio of the LSC area to the area of the needed PV cells, $G = L^2/4LH = L/4H$. Considering an FLSC of equal area (L/W fibers of length L and width W each, such that the total area is $L \times L$), we have $G \sim L/2H$, where a factor of two improvement is achieved because of the directional guiding along the fibers. This consequence of the fiber form-factor is one of the advantages of polymer FLSCs in addition to others that we describe in the following sections.

3.1. Progress in fabricating "cold" hybrid fiber structures

Traditional optical fibers typically have a circular cross section. There have been few reports of square or rectangular fibers, usually to implement novel functionalities [32,33]. The hybrid fiber structure we study here (Figure 2(c)) has an unusual cross section that has not been realized heretofore. The reliance on such a fiber structure may raise concerns, its superior performance as an FLSC notwithstanding, as to the feasibility of fabrication and hence the value of the theoretical designs and analysis pursued here. In order to address such concerns, we show in Figure 2(d)–(g) the cross sections of drawn polymer fibers we have produced demonstrating the range of control that is possible using the standard preform-to-fiber fabrication approach [23]. In all cases depicted in Figure 2(d)–(g), we draw the fibers from a scaled-up model, a "preform", in a standard fiber draw tower. In particular, note the ability to

control the height, and hence the curvature, of the cylindrical cap atop the two square fibers in Figure 2(f) and (g). The "cold" fibers are made of COP, and the cylindrical cores are PC (see the Appendix for fabrication details). Such fibers may be assembled on a flexible substrate and their ends bundled, as shown in Figure 2(h). In the doped designs we study theoretically in this paper, the core is also COP, although doped with appropriate luminescent agents. We will present our experimental results on fiber doping and FLSC efficiency measurements elsewhere [34,35].

4. IMPACT OF FLSC GEOMETRICAL AND PHYSICAL PARAMETERS ON ABSORPTION

After establishing the superior absorption performance of the hybrid capped fiber design with respect to the cylindrical and square fibers and also the feasibility of fabricating such a fiber structure, we proceed to examine the impact of the following structural and physical degrees of freedom on its performance: (i) the cylindrical-cap curvature or alternatively its height h; (ii) the optical density of the luminescent dopants α_d; (iii) the doped-core diameter D; (iv) the fiber aspect ratio $W : H$; and (v) the location of the doped core in the fiber ℓ (Figure 2(c)). We first investigate the effect of each degree of freedom separately and then carry out optimization over the full five-dimensional parameter space in Section 7. This investigation is carried out assuming a single incident wavelength and a single emission wavelength. The effect of the incident, absorption, and emission spectra is considered in Section 8.

4.1. Impact of cap height h and doping concentration α_d

Fibers with smaller h are easier to fabricate, but absorption in the core is reduced because of the resulting weaker focusing. Similarly, lowering α_d reduces the absorption of incident light, but lower values of α_d are easier to implement and also result in lower self-absorption. We assess quantitatively the impact of h and α_d on the absorption efficiency η_{abs}, defined as the fraction of incident light absorbed by the FLSC, by determining the difference between the incident optical power and the total power emerging or reflecting from the fiber.

The interplay of h and α_d is depicted in Figure 5(a). We use a monochromatic, spatially incoherent, unpolarized optical beam of uniform intensity (see the Appendix) incident normally on a hybrid fiber structure with $W = H = 500$ μm, $D = 200$ μm, and $\ell = 250$ μm. One expects that increasing α_d for fixed h will increase η_{abs}. This intuition is borne out in Figure 5(a). Note that the maximum absorption at large α_d is ultimately limited by the focusing effect of the cap.

Adding a back reflector increases η_{abs} by offering a longer effective interaction length with the dopants (Figure 5(b)). Surprisingly, the relation between η_{abs} and h is no longer monotonic for fixed α_d, as it is in the absence

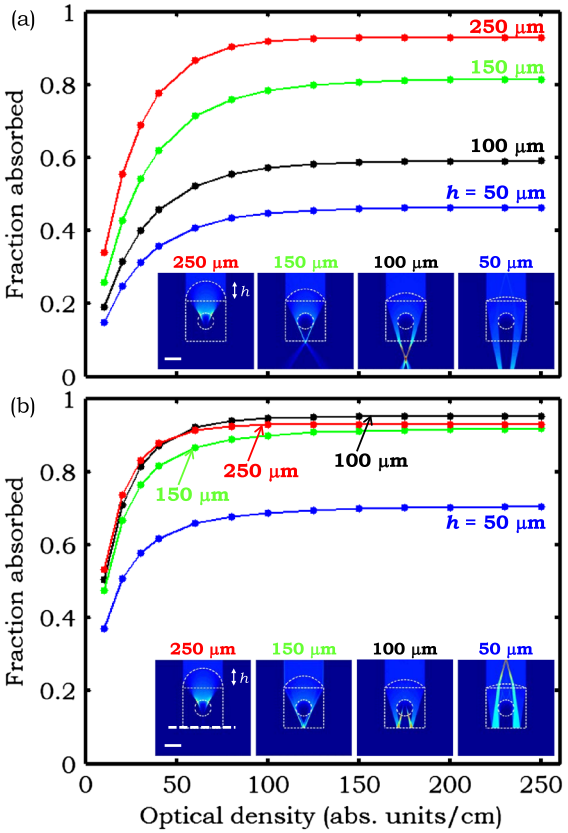

Figure 5. (a) Dependence of η_{abs} on the optical density α_d in absorbance units per unit length (centimeter)—abs. units/cm—for different cap heights: 100, 150, 200, and 250 μm. Insets show ray-tracing simulations in the four structures with $\alpha_d = 100$ cm^{-1}. (b) Same as (a) but with a back reflector provided. Scale bar in insets are both 200 μm. Here, $H = W = 500$ μm and $\ell = 250$ μm.

of the back reflector. In fact, a smaller h (e.g., 100 μm) may result in a higher η_{abs} than a larger h (150 μm) when the back reflector is added. The corresponding intensity profiles (Figure 5(b), inset) offers the explanation: While light is initially focused weaker with the lower-curvature cap, the folded-back beam has its focal point at the core, thereby increasing η_{abs} after two passes.

Finally, we plot in Figure 6 the full dependence of η_{abs} on both α_d and h in the absence and presence of a back reflector, showing that high absorption may be achieved over a wide range of values of α_d and h. Figure 5(a) and (b) are one-dimensional sections through this two-dimensional distribution.

4.2. Impact of fiber aspect ratio

It is advantageous to design an FLSC with a large aspect ratio $W : H$ by decreasing H, that is, a high-aspect-ratio rectangle. Such a structure requires less material, which reduces the weight and cost per unit area, while simultaneously increasing the flexibility of the FLSC (Figure 2(h)).

DOI: 10.1002/pip

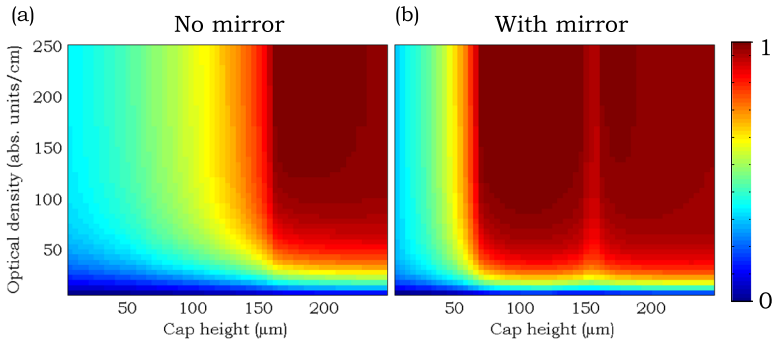

Figure 6. η_{abs} in the hybrid fiber luminescent solar concentrator structure as a function of cap height h and the optical density α_d, (a) without and (b) with a back reflector. Here, $H = W = 500$ μm and $\ell = 250$ μm. Note that η_{abs} for fixed α_d and increasing h in (b) is not monotonic as is the case in (a).

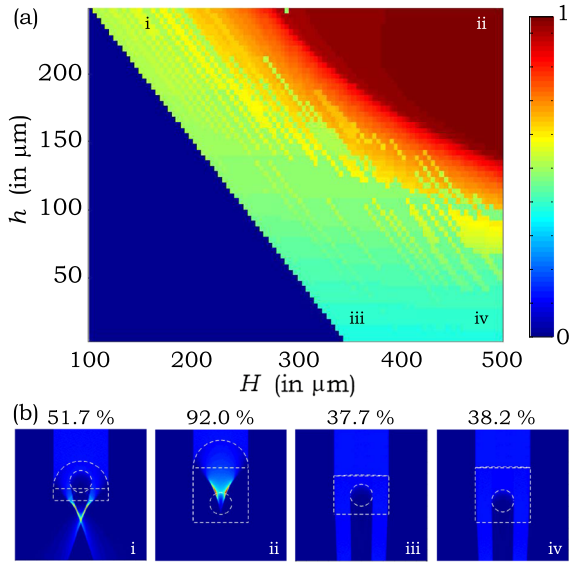

Figure 7. (a) Fraction of sunlight absorbed by a fiber luminescent solar concentrator as a function of h and H while holding the following parameters constant: $D = 200$ μm, $W = 500$ μm, and $\alpha_d = 100$ cm^{-1}. (b) Incident sunlight intensity profiles for four representative structures (i)–(iv), which are identified in (a).

We evaluate the effect of H on η_{abs} while holding W and D fixed. For each value of H, we choose the location of the core ℓ that maximizes η_{abs}. We first perform ray tracing for a cold fiber structure, determine the point with highest intensity, center the core at that point, and then carry out the ray-tracing simulation again with the doped core included. We plot in Figure 7 η_{abs} versus h and H while holding the following parameters fixed: D=200 μm, $W = 500$ μm, and $\alpha_d = 100$ cm^{-1}. The vacant part in the plot corresponds to incommensurate values of H and h, because we choose $H + h > D + 150$ to maintain a minimum of 75-μm-thick undoped polymer both below and above the doped core. We find that high absorption is achieved when large values of H and h are chosen simultaneously, and maintaining high η_{abs} while reducing H necessitates using large h.

4.3. Impact of doped-core diameter

The interplay between the effects of the doped-core diameter D and α_d on η_{abs} is shown in Figure 8. High absorption can be achieved by either increasing D or α_d in the absence or presence of a back reflector. A large core captures a wider range of focused rays for fixed α_d, and a higher α_d results in stronger absorption for fixed D. Unfortunately, configurations that result in the highest η_{abs}, such as those with large D or high α_d, usually also induce high self-absorption, as we shall see shortly. Thus, in choosing the values of such degrees of freedom, a compromise must be struck between improving η_{abs} and self-absorption, which reduces the luminescence reaching the FLSC end.

5. LUMINESCENCE CAPTURE IN THE FIBER

A fraction of the absorbed optical energy is lost because of the luminescence quantum efficiency of the dopants (non-radiative decay of the excited state) and the quantum defect (the Stokes shift between the absorbed and emitted wavelengths). These two effects are captured in the parameter η_Q, the quantum conversion efficiency, which is the fraction of absorbed optical energy that is re-emitted into the fiber. In this section, we determine the fraction of the *emitted* radiation that is confined in the fiber via TIR (η_{TIR}). The remaining fraction, emitted in the so-called escape cone, leaks out. This captured fraction depends on the refractive index and the fiber geometry. While analytic formulae for η_{TIR} have been derived for simple geometries such as slab and circular waveguides [21], we estimate η_{TIR} in our hybrid FLSC geometry by ray-tracing simulations.

We compare η_{TIR} in the square, cylindrical, and hybrid FLSCs by scanning a luminescent point source (1-μm radius) emitting isotropically 50,000 rays/μm^2 ($\sim$ 157,000 rays per point source) and determine the remaining fraction of rays confined in the cold fiber after the

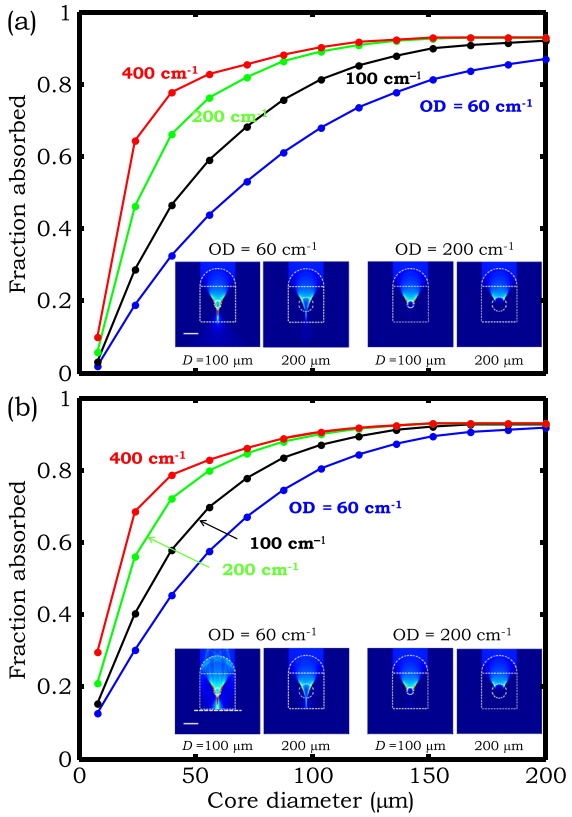

Figure 8. Impact of D and α_d on η_{abs} for fiber luminescent solar concentrators (a) without and (b) with a back reflector. The insets in (a) and (b) show the incident sunlight intensity profiles for four representative structures. Here, $H = W = 500$ μm and $\ell = 250$ μm.

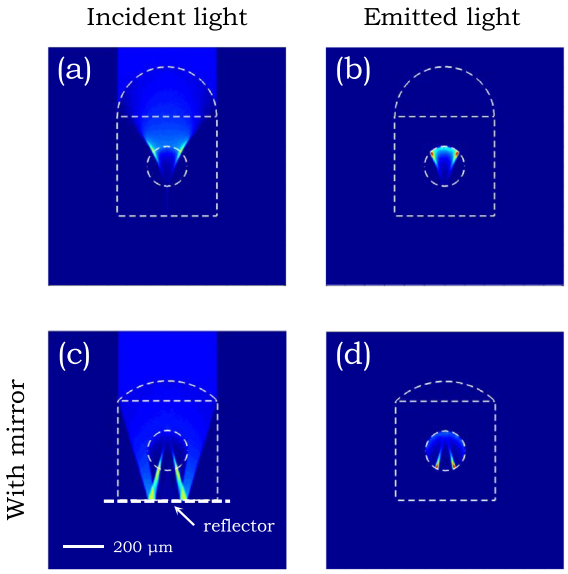

Figure 9. Intensity profile of incident sunlight in a fiber luminescent solar concentrator (FLSC) with (a) $H = W = 500$ μm, $\ell = 250$ μm, $D = 200$ μm, $h = 250$ μm, $\alpha_d = 100$ cm^{-1}, and (c) $H = W = 500$ μm, $\ell = 250$ μm, $D = 200$ μm, $h = 100$ μm, $\alpha_d = 100$ cm^{-1}. (b) and (d) are the luminescence emission profiles corresponding to the FLSCs in (a) and (c).

unguided rays have leaked out, which typically occurs in less than 1 mm. Although dye molecules in a solid matrix (for example) may retain the memory of the optical excitation, and hence signatures of the dipole molecular emission may be observed [36,37], the incoherence and unpolarized nature of solar radiation justifies the assumption of isotropic emission.

For a rectangular waveguide with $n = 1.53$, we find that $\eta_{TIR} \approx 50.8\%$ independently of the emission position of the point source and of the aspect ratio $W : H$ (see Ref. [21]). In a cylindrical waveguide of the same refractive index, η_{TIR} for a point source that is scanned in the radial direction changes from $\approx 34.6\%$ for an on-axis emitter to $\approx 75.5\%$ for a point source located at the surface. In the hybrid FLSC, η_{TIR} changes with h from 50.8% when $h = 0$ (rectangular fiber) and drops rapidly to 34.6% when $h = 50$ μm, and remains so with increase in h to a maximum value of $h = 250$ μm (here $W = H = 500$ μm).

Crucially, η_{TIR} is independent of position in the hybrid FLSC, similarly to the rectangular fiber and in contradistinction to the cylindrical fiber. This allows us to implement a very useful simplification: There is no need to simulate the propagation along each structure with its distinct non-uniform luminescence emission profile, which is proportional to the intensity of light absorbed locally. Two examples of such spatially varying emission profiles are shown in Figure 9. Instead of using directly these profiles, we may replace an arbitrarily shaped emission pattern with an isotropically emitting *uniform disc* having the same diameter as the doped core, with the proviso that the total luminescence power of this unform disc is equal to that of the original spatially varying emission profile. We hereon use this simplification, which enables us to reach general conclusions in the next section with regard to self-absorption.

6. IMPACT OF SELF-ABSORPTION

Self-absorption is the suppression of the useful output signal resulting from the unavoidable overlap between the absorption and emission spectra of the luminescent dopants, and it typically sets the upper limit on useful LSC size and performance [2,6]. Two material properties help quantify self-absorption: (i) the Stokes shift $\Delta\lambda_S$, which is the difference between the peak absorption λ_A and the peak emission $\lambda_{PL} = \lambda_A + \Delta\lambda_S$ wavelengths, and (ii) the self-absorption ratio S, the ratio between the absorption coefficient values at peak absorption and peak emission wavelengths $S = (\Phi_a(\lambda_A))/(\Phi_a(\lambda_{PL}))$, where $\Phi_a(\lambda)$ is the absorption spectrum. In an ideal LSC, $\Delta\lambda_S$ and S should be as large as possible. In this section, we use the param-

eters typical of a laser dye in a solid matrix as a model luminescent material ($S=100$).

While simplified analytical models for self-absorption in planar [2] and cylindrical [22] LSCs have been developed, the unusual cross section of our FLSC necessitates the use of simulations to evaluate the impact of self-absorption. We consider here only the first generation of luminescent photons; that is, re-emission after self-absorption is neglected. Consequently, the spectral red shift resulting from multiple emission/re-absorption events is ignored.

It is expected that self-absorption increases with propagation distance z along the FLSC, with α_d, and with the doped area in the FLSC cross section. We define a figure of merit η_{sa}, which is the fraction of emitted luminescence that reaches the fiber end after undergoing self-absorption. We have performed simulations in the four-dimensional parameter space of H, h, D, and α_d, and the results reveal that η_{sa} may be accurately modeled by an exponential function of the form

$$\eta_{sa}(z) = e^{-\kappa\cdot\alpha_d(\lambda_e)\cdot A_r\cdot z} \quad (1)$$

where A_r is the fraction of the cross-sectional area that is (uniformly) doped, α_d is the optical density of the doped region at the *emission* wavelength λ_e, and z is the axial position along the FLSC away from the point where incident radiation is absorbed. Here, $\kappa = 3.064$ is an empirical fitting parameter that results in an average error in estimating η_{sa} of $\sim$ 1% averaged over all the examined configurations.

7. OPTIMUM FLSC PERFORMANCE

The overall optical conversion efficiency η_O is a product of the efficiencies of the consecutive processes we have discussed thus far,

$$\eta_O(z) = (1-R)\times\eta_{abs}\times\eta_Q\times\eta_{TIR}\times\eta_{prop}(z) \quad (2)$$

here z is the distance along the fiber measured from the position of incident light confined to a point; R is the fraction of sunlight reflected from the fiber outer surface (Section 3); η_{abs} is the fraction of sunlight absorbed by the luminescent materials (Section 4); η_Q is the quantum conversion efficiency, which incorporates the luminescence quantum efficiency and the quantum defect (Section 5); η_{TIR} is the fraction of luminescence confined by TIR (Section 5); and η_{prop} is the fraction of trapped luminescence delivered to the fiber tip after absorption by the host, waveguide losses due to surface roughness, and self-absorption (Section 6),

$$\eta_{prop}(z) = \eta_{host}(z)\times\eta_r(z)\times\eta_{sa}(z) \quad (3)$$

The three factors in Equation (3) all typically have the form of an exponential function, but the exponent of η_{sa} (Equation (1)) usually dominates.

The overall optical conversion efficiency is obtained by integrating $\eta_O(z)$ over the length of the fiber L:

$$\eta_O = (1-R)\times\eta_{abs}\times\eta_Q\times\eta_{TIR}\times\int_0^L dz\,\eta_{prop}(z) \quad (4)$$

This formula corresponds to integrating the amount of light reaching the fiber ends from a set of incident points distributed uniformly along its length.

Now that we have in place all the elements of a full model of our FLSC, we carry out an optimization of its performance with respect to its degrees of freedom. We simulate more than 52,000 FLSC configurations using the full model in search of the maximum optical concentration efficiency η_O, defined as the fraction of normally incident optical energy that is delivered to the fiber end in the form of luminescence. We fix the following FLSC parameters: length is L = 30 cm, S = 100 (a conservative value; e.g., DCJTB has $S \sim 180$ in a typical solid matrix), and W = 500 μm. The FLSC parameters we vary are (i) α_d in the range 0 to 400 cm^{-1}; (ii) D in the range 8 to 200 μm; (iii) h in the range 4 to 250 μm; and (iv) H in the range $D-h+150$ to W.

We find a maximum efficiency of η_O = 13.92% for a configuration with α_d = 340 cm^{-1}, D = 24 μm, H = W = 500 μm, and h = 250 μm. When the FLSC is provided with a reflective mirror, a maximum efficiency η_O = 14.16% occurs for a configuration with α_d = 280 cm^{-1}, D = 24 m, W = H = 500 μm, and h = 100 μm. Although the optimal efficiencies are similar in the presence and absence of the mirror, the optimal value in the former requires a smaller cap height h and a lower doping concentration α_d, which ease fabrication constraints.

8. INTEGRATION OVER THE SOLAR AND LUMINESCENCE SPECTRA

The ray-tracing simulations reported earlier are carried out assuming incident radiation at a single wavelength and a single emission wavelength. We now move to a more realistic model where three relevant spectral distributions are incorporated: (i) the incident radiation has a spectral distribution $\Phi_i(\lambda)$, taken to be AM 1.5 solar spectrum; (ii) the absorption spectrum of the luminescent dopants is $\Phi_a(\lambda)$; and (iii) their emission spectrum is $\Phi_e(\lambda)$. We normalize these three spectra such that $\int d\lambda\Phi_j(\lambda) = 1$, where j = i, a, e.

We now generalize the results in the previous sections by integrating η_O over all three spectra using the formula

$$\eta_O = (1-R)\times\eta_{TIR}\times\eta_Q\times\int d\lambda_i\,\eta_{abs}(\lambda_i)\Phi_i(\lambda_i)\times\int_0^L dz\int d\lambda_e\,\eta_{prop}(\lambda_e,z)\Phi_e(\lambda_e)$$

where λ_i and λ_e are the incident and emitted wavelengths (see, e.g., Ref. [38]). This formula captures a very general model of an FLSC with the parameters of the incident light, the fiber, and the luminescent materials included. Note that both η_{prop} and η_{abs} are now wavelength-dependent at the absorption and emission wavelengths through $\alpha_d(\lambda) = \alpha_d^{(peak)}\Phi_a(\lambda)$, where $\alpha_d^{(peak)}$ is a scaling factor for the normalized distribution $\Phi_a(\lambda)$. We ignore the wavelength dependence of η_{TIR}, which amounts to neglecting the polymer material dispersion in the wavelength range of interest, which is a minor effect.

In performing this spectral integration, we use a simplified model for $\Phi_a(\lambda)$ formed by the superposition of two Gaussian spectra

$$\Phi_a(\lambda) = \frac{1}{2\sqrt{2\pi\sigma_a^2}}\left\{\exp\left(-\frac{(\lambda-\lambda_1)^2}{2\sigma_a^2}\right) + \exp\left(-\frac{(\lambda-\lambda_2)^2}{2\sigma_a^2}\right)\right\} \quad (5)$$

with peaks at $\lambda_1 = 400$ nm and $\lambda_2 = 550$ nm, and full-width half-maximum bandwidths of 120 nm each. This model represents the absorption spectrum of a broadband absorbing fluorescent dye or a compound fluorescent material. We take $\Phi_e(\lambda)$ to have a Lorentzian distribution,

$$\Phi_e(\lambda) = \frac{1}{2\pi}\frac{\sigma_e}{(\lambda-\lambda_3)^2 + \frac{1}{2}\sigma_e^2} \quad (6)$$

with emission peak at $\lambda_3 = 730$ nm and full-width half-maximum bandwidth $\sigma_e = 15$ nm (Figure 10(a)). In designing an ideal LSC in general, the goal is to choose materials with the broadest spectral distribution for $\Phi_a(\lambda)$ to capture the solar spectrum, while minimizing the overlap between $\Phi_a(\lambda)$ and $\Phi_e(\lambda)$ to reduce self-absorption.

Using the optimal geometrical configuration in the previous section ($H = W = 500$ μm, $D = 24$ μm, and no back reflector), we searched for the optical density of luminescent dopants $\alpha_d^{(peak)}$ that maximizes η_O when the full spectral integration is carried out. We extended the range of $\alpha_d^{(peak)}$ to 2000 cm^{-1} because the increase of absorption at higher $\alpha_d^{(peak)}$ outstrips the increase in self-absorption after spectral averaging beyond the value 400 cm^{-1} we used in Section 7.

Figure 10(b) depicts the dependence of η_O on $\alpha_d^{(peak)}$ and FLSC length. For this FLSC geometry, maximal values for two different fiber lengths $L = 2.5$ and 30 cm are η_O of 7.2% and 6.2%, which occur at $\alpha_d^{(peak)} = 1670$ and 967 cm^{-1}, respectively. We further multiply these values by 0.7 to account for several factors that contribute to the reduction in overall FLSC system efficiency.

(1) Power-conversion efficiency at the PV cells attached to the FLSC ends. We assume PV cells are selected such that their peak conversion efficiency occurs in a spectral band that overlaps with the emission spectra of the luminescent dopants. Close-to-unity conversion efficiency may be achieved in this fashion (see Ref. [39]).
(2) Coupling losses from the fiber ends to the PV cell. These losses can be minimized using clear index-matching optical glues.
(3) Non-unity η_Q for real luminescent dopants. η_Q greater than 0.95 is common in fluorescence dyes and quantum dots.

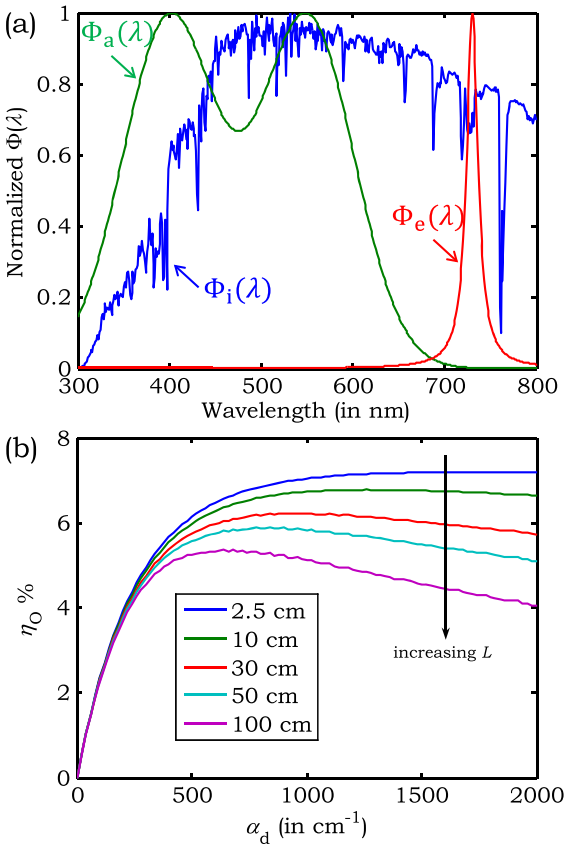

Figure 10. (a) The three spectral distributions used in our simulation model: incident AM 1.5 solar spectrum Φ_i, absorption spectrum Φ_a, and emission spectrum Φ_e. The three spectra are each normalized to their peak for clarity. (b) η_O as a function of optical density of luminescent dopants $\alpha_d^{(peak)}$ for different fiber luminescent solar concentrator lengths L. The FLSC parameters chosen here are those for the single-wavelength optimal structure in Section 7: $H = W = 500$ μm, $D = 24$ μm, and no back reflector.

The conservative multiplicative factor of 0.7 reduces the potential optical-to-electrical power conversion efficiencies to $\eta_{conv} = 5.0\%$ and 4.3% for FLSC lengths of 2.5 ($G = 18$) and 30 cm ($G = 220$), respectively.

For comparison with conventional flat slab LSCs, we use Ref. [2] where $\eta_{conv} = 6.8\%$ was estimated from measurements of η_O on a small-area, thick LSC of dimensions $25 \times 25 \times 2$ mm^3 ($G = 3$). Currie *et al*. [2] projected a reduction to $\eta_{conv} = 6.1\%$ for an LSC having $G = 45$ (surface area of 36×36 cm^2). The values in Ref. [2], however, were obtained using a high-index glass (SF10, $n = 1.8$), which improves η_{TIR} by 27% over the polymer FLSC here ($n = 1.53$). By incorporating this effect, we find that the calculated values of η_{conv} here for an FLSC and the reported values for a slab LSC are comparable, although while achieving much larger values of G in the FLSC having the same area as the slab LSC.

9. SUMMARY AND CONCLUSION

While the proposed polymer FLSC structure yields comparable values of η_{conv} to those of state-of-the-art glass-based slab LSCs, there are nevertheless several advantages that suggest the usefulness of FLSCs. First, polymer-based FLSCs are lighter-weight than glass-based LSCs. For example, the density of SF10 glass (used in Ref. [2]) is 4.8 g/cm^3, compared with 1.02 g/cm^3 for COP. Using the dimensions $W = H = 500$ μm and $h = 250$ μm for the FLSC and the dimensions in Ref. [2], the weight of the FLSC per unit area is reduced by a factor of ≈ 13.5. The FLSC fabric is projected to weigh only ≈ 700 g/m^2. The superior mechanical properties of polymers versus glasses with respect to bending forces further suggest the usefulness of FLSCs in mobile applications.

Finally, FLSCs may improve the economics of solar energy because the cost of unit power generated by a concentrator is directly proportional to the cost of collector system and inversely proportional to the product $G \times \eta_{conv}$ (see Equation (1) of Ref. [2]). The larger G for the FLSC's designs investigated here (but with comparable η_{conv}) means that both the smaller-area PV cells are required and the smaller quantity of polymer is needed in constructing the FLSC compared with a glass-based slab LSC of the same area. The cost is reduced on all three counts, thereby potentially reducing the cost by an order of magnitude.

Future investigations will examine the performance of these FLSCs with respect to diffuse incident light and the potential of combining both the down-conversion and up-conversion materials to harness the full solar spectrum. Our experimental results on FLSC fabrication and characterization will be presented elsewhere [34,35].

In conclusion, we have presented a full investigation of the design of a luminescent solar concentrator having the form-factor of a fiber, an FLSC. We have examined the impact of the geometric and physical degrees of freedom of the FLSC on its performance. Such FLSCs may be readily fabricated using the traditional and scalable process of thermal drawing. These new concentrators offer several unique advantages in terms of weight and flexibility without sacrificing the performance in comparison with state-of-the-art glass-based slab LSCs.

ACKNOWLEDGEMENT

This work was funded by the US Air Force Office of Scientific Research (AFOSR) under contract FA-9550-12-1-0148.

REFERENCES

1. Debije MG, Verbunt PPC. Thirty years of luminescent solar concentrator research: Solar energy for the built environment. *Advanced Energy Materials* 2012; **2**: 12–35.
2. Currie MJ, Mapel JK, Heidel TD, Goffri S, Baldo MA. High-efficiency organic solar concentrators for photovoltaics. *Science* 2008; **321**: 226–228.
3. Barnham K, Marques JL, Hassard J, O'Brien P. Quantum-dot concentrator and thermodynamic model for the global redshift. *Applied Physics Letters* 2000; **76**: 1197–1199.
4. Purcell-Milton F, Gun'ko YK. Quantum dots for luminescent solar concentrators. *Journal of Materials Chemistry* 2012; **22**: 16687–16697.
5. Wang T, Zhang J, Ma W, Luo Y, Wang L, Hu Z, Wu W, Wang X, Zou G, Zhang Q. Luminescent solar concentrator employing rare earth complex with zero self-absorption loss. *Solar Energy* 2011; **85**: 2571–2579.
6. Batchelder JS, Zewail AH, Cole T. Luminescent solar concentrators. 1: Theory of operation and techniques for performance evaluation. *Applied Optics* 1979; **18**: 3090–3110.
7. Batchelder JS, Zewail A H, Cole T. Luminescent solar concentrators. 2: Experimental and theoretical analysis of their possible efficiencies. *Applied Optics* 1981; **20**: 3733–3754.
8. Weber WH, Lambe J. Luminescent greenhouse collector for solar radiation. *Applied Optics* 1976; **15**: 2299–2300.
9. Farrell DJ, Yoshida M. Operating regimes for second generation luminescent solar concentrators. *Progress in Photovoltaics* 2012; **20**: 93–99.
10. Bomma J, Büchtemann A, Chatten AJ, Bose R, Farrell DJ, Chan NLA, Xiao Y, Slooff LH, Meyer T, Meyer A, van Sark WGJHM, Koole R. Fabrication and full characterization of state-of-the-art quantum dot luminescent solar concentrators. *Solar Energy Materials and Solar Cells* 2011; **95**: 2087–2094.

11. Shcherbatyuk GV, Inman RH, Wang C, Winston R, Ghosh S. Viability of using near infrared PbS quantum dots as active materials in luminescent solar concentrators. *Applied Physics Letters* 2011; **96**: 191901.
12. Mulder CL, Reusswig PD, Velázquez AM, Kim H, Rotschild C, Baldo MA. Dye alignment in luminescent solar concentrators: I. Vertical alignment for improved waveguide coupling. *Optics Express* 2010; **18**: A79–A90.
13. MacQueen RW, Cheng YY, Clady RGCR, Schmidt TW. Towards an aligned luminophore solar concentrator. *Optics Express* 2010; **18**: A161–A166.
14. McDowall S, Johnson BL, Patrick DL. Simulations of luminescent solar concentrators: Effects of polarization and fluorophore alignment. *Journal of Applied Physics* 2010; **108**: 053508.
15. Slooff LH, Bende EE, Burgers AR, Budel T, Pravettoni M, Kenny RP, Dunlop ED, Büchtemann A. A luminescent solar concentrator with 7.1 % power conversion efficiency. *Physica Status Solidi* 2008; **2**: 257–259.
16. Kennedy M, McCormack SJ, Doran J, Norton B, In *Proc. ISES World Solar Congress*, Beijing, China, 2007; 1484–1488.
17. Tsoi S, Broer DJ, Bastiaansen CWM, Debije MG. Patterned dye structures limit reabsorption in luminescent solar concentrators. *Optics Express* 2010; **18**: A536–A543.
18. Wang S -Y, Borca-Tasciuc D -A, Kaminski DA. Spectral coupling of fluorescent solar concentrators to plasmonic solar cells. *Journal of Applied Physics* 2011; **109**: 074910.
19. Giebink NC, Wiederrecht GP, Wasielewski MR. Resonance-shifting to circumvent reabsorption loss in luminescent solar concentrators. *Nature Photonics* 2011; **5**: 694–701.
20. Yoon J, Li L, Semichaevsky AV, Ryu JH, Johnson HT, Nuzzo RG, Rogers JA. Flexible concentrator photovoltaics based on microscale silicon solar cells embedded in luminescent waveguides. *Nature Communications* 2011; **2**: 343.
21. Mcintosh K, Yamada N, Richards B. Theoretical comparison of cylindrical and square-planar luminescent solar concentrators. *Applied Physics B* 2007; **88**: 285–290.
22. Wu W, Wang T, Wang X, Wu S, Luo Y, Tian X, Zhang Q. Hybrid solar concentrator with zero self-absorption loss. *Solar Energy* 2010; **84**: 2140–2145.
23. Abouraddy AF, Bayindir M, Benoit G, Hart SD, Kuriki K, Orf N, Shapira O, Sorin F, Temelkuran B, Fink Y. Towards multimaterial multifunctional fibres that see, hear, sense and communicate. *Nature Materials* 2007; **6**: 336–347.
24. Scudo PF, Abbondanza L, Fusco R, Caccianotti L. Spectral converters and luminescent solar concentrators. *Solar Energy Materials and Solar Cells* 2010; **94**: 1241–1246.
25. Chatten AJ, Farrel D, Jermyn C, Thomas P, Buxton BF, Buchtemann A, Barnham KW, In *Proc. 31st IEEE Photovoltaic Specialists Conference*, New York, 2005; 82–85.
26. Nunes PS, Ohlsson PD, Ordeig O, Kutter JP. Cyclic olefin polymers: emerging materials for lab-on-a-chip applications. *Microfluidics and Nanofluidics* 2010; **9**: 145–161.
27. Debije MG, Broer DJ, Bastiaansen CWM. Effect of dye alignment on the output of a luminescent solar concentrator. In *Proc. 22nd European Photovoltaics Solar Energy Conference*, Willeke G, Ossenbrink H, Helm P (eds). WIP: Munich, Germany, 2007; 87–89.
28. Mulder CL, Reusswig PD, Beyler AP, Kim H, Rotschild C, Baldo MA. Dye alignment in luminescent solar concentrators: II. Horizontal alignment for energy harvesting in linear polarizers. *Optics Express* 2010; **18**: A91–A99.
29. http://www.zeonex.com/datasheets.asp [Last accessed 11/01/2013].
30. Yamashita T, Kamada K. *Japanese Journal of Applied Physics* 1993; **32**: 2681.
31. Tsoi S, Broer DJ, Bastiaansen CWM, Debije MG. Using lenses to improve the output of a patterned luminescent solar concentrator. *Advanced Energy Materials* 2013; **3**: 337–341.
32. Hayes JR, Flanagan JC, Monro TM, Richardson DJ, Grunewald P, Allott R. Square core jacketed air-clad fiber. *Optics Express* 2006; **14**: 10345–10350.
33. Egusa S, Wang Z, Chocat N, Ruff ZM, Stolyarov AM, Shemuly D, Sorin F, Rakich PT, Joannopoulos JD, Fink Y. Multimaterial piezoelectric fibres. *Nature Materials* 2010; **9**: 643–648.
34. Banaei E -H, Abouraddy AF. Polymeric fiber luminescent solar concentrators 2013, in preparation.
35. Banaei E -H. *Ph.D. Thesis*, University of Central Florida, 2013.
36. Schafer FP. *Dye Lasers*. Springer-Verlag: Berlin, 1989.
37. Shapira O, Kuriki K, Orf N, Abouraddy AF, Benoit G, Viens J, Rodriguez A, Ibanescu M, Joannopoulos JD, Fink Y, Brewster MM. Surface-emitting fiber lasers. *Optics Express* 2006; **14**: 3929–3935.
38. Earp AA, Franklin JB, Smith GB. Absorption tails and extinction in luminescent solar concentrators. *Solar Energy Materials and Solar Cells* 2011; **95**: 1157–1162.
39. Fisher B, Biddle J. Luminescent spectral splitting: Efficient spatial division of solar spectrum at low concentration. *Solar Energy Materials and Solar Cells* 2011; **95**: 1741–1755.

APPENDIX

Ray-tracing simulations—We carried out our modeling and optimization simulations using the Monte Carlo ray-tracing software package ZEMAX® in the non-sequential mode in conjunction with MATLAB®. We employ ray tracing in lieu of the beam-propagation method, for instance, because of the large bandwidth of the radiation in k-space in conjunction with the typical sizes of FSLCs under investigation ($\sim 10^6\lambda^2$), which makes beam-propagation methods computationally prohibitive. We account for the effects of the angles of incidence and polarization on reflection and refraction at interfaces through the use of the "polarization ray-tracing" method.

The fiber structures are defined by either overlapping simple geometrical shapes or extruding objects through user-defined apertures. This allows us to set the *geometric* parameters of the cross section, such as width W and height H of the rectangular section, the cylindrical cap height h, and diameter D and location ℓ of the core. The *physical* parameters of the fiber, such as the wavelength-dependent refractive index $n(\lambda)$ and the optical absorption coefficient $\alpha(\lambda)$ of the luminescent dopants, are also adjusted. The polymer refractive index throughout the visible was fixed at its value at 550 nm, thereby in effect neglecting material dispersion for the polymer. Furthermore, ray-tracing calculations over a set of fiber structures in which a geometric or physical parameter is scanned over a range of values is carried out in a loop using macros written in the ZEMAX programming language (ZPL).

The incident light throughout the paper is assumed to be spatially incoherent and unpolarized. The source is a rectangle of dimensions $500 \times 100\ \mu m^2$ producing collimated rays with unity radiation power illuminating the fibers vertically from the top. Simulations to estimate the percentage of incident sunlight absorbed by the fiber make use of a source producing 10,000 rays. Increasing the number of rays to 200,000 in these simulations changes the estimated absorption percentage by less than % 0.01.

To estimate the power absorbed by the "cold" fiber (Figure 3), we place flat detectors surrounding all sides of the fiber to detect light emerging from it. The percentage of absorbed light is the difference between the source and the detected signal. In order to obtain the intensity distribution inside the fibers, we place a detector normal to the fiber axis at the location of interest tilted 1° with respect to that normal. The detector intercepts the rays at the plane of interest while introducing minimal distortion in the acquired distribution. To isolate the desired absorption by the luminescent dopants from background absorption of the host polymer, all materials in the doped fibers except the luminescent dopants were assumed lossless for the simulations, and the host material absorption was subsequently added separately. For the case of doped cores, we utilize the "bulk scattering" feature of ZEMAX®, which simulates fluorescence in ray tracing.

To simulate the propagation of the captured fraction of light axially along the fiber, ray-tracing simulations were performed. We used ray tracing in lieu of the beam-propagation method that is usually applied in optical fiber configurations but is less appropriate in the case of an FLSC. The reason is that the luminescence is emitted over a wide range of angles—even after eliminating light within the escape cone. In beam-propagation method, the grid resolution in the transverse plane has to be fine enough to allow the largest transverse k-vector components to be still far away from the boundaries of the simulation window in k-space. This constraint makes beam propagation calculations of luminescence in FLSCs of the size described here extremely time-consuming. Because the fiber dimensions are much larger than optical wavelengths, we choose to rely on ray tracing using a ray density of 5 rays/μm^2 in the luminescing core, as described in the main text. We monitor the fraction of emitted light that remains confined within the fiber as a function of length while varying the FLSC degrees of freedom, which led to developing the empirical model presented in Equation (1).

The ability to absorb and concentrate diffuse light is one of the major advantages of flat LSCs in general. In the FLSC described here, the flat symmetry is broken, and two new symmetry axes emerge: one symmetry axis runs along the fiber, while the other symmetry axis is transverse to the fiber. Incident diffuse light falls within a cone of angles whose axis is normal to the fiber (the vertical direction here) and with principal axes aligned with the two new symmetry axes. Our FLSC design retains completely the advantages accrued by traditional LSCs for diffuse light with angular spread along the symmetry direction parallel to the fiber axis. That is, light inclined with respect to the fiber axis but lying in a plane formed of the vertical direction and the fiber axis is captured in an identical fashion to the normal rays examined in our simulations. This advantage is partially compromised along the orthogonal direction in the specific simple fiber design studied here. The larger the doped core diameter or the smaller the lens cap height, the less pronounced this effect will be. We have tested this hypothesis quantitatively by performing ray-tracing simulations on an FLSC with suboptimal parameters: $H = W = 500\ \mu m$, $h = 250\ \mu m$, and $D = 120\ \mu m$. The percentage of rays intercepting the doped core drops from 93% to 57% by changing the incident angle from normal to 10° with respect to normal for an individual fiber with only the fiber curved cap surface illuminated. The situation may be improved by taking two measures: increasing the core diameter or by including multiple small-diameter cores in the transverse cross section to increase the external geometric acceptance angle along the direction impacted by the fiber broken symmetry.

The sole purpose of adding the back reflector is to reflect back incident sunlight that was not absorbed upon the first pass through the fiber. The goal therefore is *not* for this reflector to contribute to the optical guidance of

the luminescence,but only to increase the transverse interaction length between incident sunlight and the dopants in the core. Indeed, imperfect reflection from the mirror results in considerable loss in the transport of luminescence if the mirror is in contact with the waveguide, thereby necessitating that one incorporates an air gap between the fiber and the reflective surface. Adding a mirror—and an associated air gap—to the proposed fiber system will of course incur further system complexity. An emerging technology for transparent or reflective adhesive films has been recently developed for Organic light emitting diodes (OLEDs) and other applications (e.g., United States Patent 8427747), in which low-index adhesive material is applied to narrow regions forming adhesive strips or squares. Such films may address the need in our scenario. Alternatively, modified fiber cross sections can be envisioned with slightly protruding or pronounced edges such that the majority of the fiber bottom surface is not in touch with the reflective surface. The results of our simulations presented here demonstrate that FLSCs with and without the back reflector achieve similar total optical efficiencies at the price of higher concentration of dopants needed and larger core diameter in the case of the FLSC without a back reflector. Thus, while the back reflector would be helpful, if it proves not to be feasible on a practical level, the proposed FLSC will still function with a similar total efficiency.

"Cold" fiber fabrication—Figure 2(d)–(g) demonstrates the feasibility of thermal drawing of polymer fibers even when unusual cross-sectional structures are desired, such as the hybrid fiber shown in Figure 2(c). The cold fibers shown in Figure 2(d)–(g) are fabricated as follows. Carefully cleaned PC (LEXAN 104 from SABIC innovative plastics) granules are heated to 240 °C and extruded under vacuum into a solid rod that is used as the preform core. Cleaned COP (Zeonor 1420R from Zeon Chemicals) 75-μm-thick polymer films are tightly rolled around the PC rod and then consolidated under vacuum at 180 °C. The consolidated preforms, consisting of a cylindrical PC core and concentric cylindrical COP cladding, are subsequently machined into the desired forms for the square (Figure 2(e)) or hybrid (Figure 2(f) and (g)) fibers. No core was provided in the hybrid fiber structure shown in Figure 2(g). The preforms are then thermally drawn in a fiber draw tower [23]. As can be seen in Figure 2, except for slight deformations in the fiber cross section that occur during the drawing process, the overall geometry of the preform is controllably reproduced in the fiber. Our results on controlled doping with luminescent agents will be reported elsewhere [34,35].

DOI: 10.1002/pip